Visualization of Local Ionic Concentration and Diffusion Constants Using a Tailored Electrochemical Strain Microscopy Method

M. Simolka, [1] C. Heim,[2] K. A. Friedrich, [3,*,z] and R. Hiesgen [1,†,*]

[1]University of Applied Sciences Esslingen, Department of Basic Science, D-73728 Esslingen, Germany
[2]German Aerospace Center (DLR), Institute of Engineering Thermodynamics, D-70569 Stuttgart, Germany
[3]Institute of Energy Storage, University of Stuttgart, 70569 Stuttgart, Germany

A tailored electrochemical strain microscopy technique is presented and used to analyze the ionic mobility and diffusion coefficients in composite Si/C anodes. The resulting surface displacement after a voltage pulse is proportional to the ionic concentration change and is measured by the deflection of an atomic force microscopy tip. The results show a higher ionic mobility at the steps of silicon composite anode microcrystals compared to the crystal centers. Diffusion coefficients are extracted from the time dependence of the surface displacement. Mappings with nanoscale resolution of local diffusion coefficients are displayed. The results demonstrate higher diffusion coefficients at the steps.

The further development of Li ion batteries from an already advanced technology base requires information of local properties such as Li ion concentration, mobility, and diffusion coefficients on nanometric scales. For this purpose, the available analyses are not adequate and the research community needs to implement novel methods. For the characterization of aging mechanisms and the diffusion coefficients of ions, several techniques are available. Examples are electrochemical impedance spectroscopy (EIS), differential voltage analysis (DVA), incremental capacity analysis (ICA), current pulse techniques, potentiostatic and galvanostatic intermittent titration techniques (PITT and GITT), or imaging such as scanning electron microscopy (SEM). These techniques either work on the battery cell level and do not resolve the local degradation of the material down to microscopic scales, or only analyze the material surface and composition. On the nanometer scale, atomic force microscopy (AFM) is an imaging technique with high resolution, even down to the scale of atoms.[1] Besides the surface morphology, it delivers information on the generation of surface layers as well as local material- and electrical properties of the samples. Aurbach et al. used in-situ AFM in a glove-box to study the deposition processes, surface layer generation in several electrolytes, and electrode degradation.[2–5] Elazari et al. and Hiesgen et al. showed for lithium-sulfur electrodes a change of the material properties with cycling and a decrease of the electric conductivity in the electrodes.[6,7] Doi et al. conducted electrochemical AFM on $LiMn_2O_4$ and reported a rapid change of the surface in contact with electrolyte and the development of a surface layer with small particles.[8] McAllister et al. investigated silicon as a battery anode material and observed the pulverization and changes in material properties due to lithiation.[9] Clémonçon et al. studied the surface and dimensional changes of $LiCoO_2$. They reported the surface expansion along one crystal axis during lithiation of $LiCoO_2$ and revealed the electrochemical surface stability up to 4.2 V vs Li/Li$^+$.[10] Zhu et al. investigated TiO_2 as an anode material for Li ion batteries using Kelvin probe force microscopy (KPFM). They measured changes in the surface potential due to Li ion insertion and extraction and observed charge accumulation at grain boundaries.[11] Martin et al. studied structural and stability dependency of electrolyte additives on the solid electrolyte interface (SEI) at silicon anodes using AFM. Their study showed the positive influence of vinylene carbonate (VC) as an electrolyte additive on the stability of the SEI.[12]

Electrochemical strain microscopy (ESM), a special contact AFM mode, and its derivative techniques are a powerful tool for material scientists for the analysis of local ionic concentration and the ionic mobility down to the nanometer level. Analysis of the distribution of concentration and the ionic mobility inside the material can help to improve the cycle life of battery cells, since aging mechanisms such as lithium plating and the increase of the electrode impedance are initiated by inhomogeneous material distribution and a decrease of ionic kinetics.[13,14] The ESM technique was first introduced by Balke et al.; the theoretical background was proposed by Balke et al., and Morozovska et al.[15–19] Two other AFM techniques for the detection of the ionic distribution were developed. The first mode is called scanning thermo-ionic microscopy (STIM), it was proposed by Eshghinejad et al., but has not received much attention yet.[20,21] It uses thermal excitation of the ions in combination with a lock-in technique to analyze their distribution. The second mode, KPFM, measures the surface potential of the material, which is influenced by the electrochemical potential of ions. Using KPFM, Zhu et al., and Luchkin et al. demonstrated the potential difference in lithiated and non-lithiated materials.[11,22] These techniques have the disadvantage that they do not provide any information on the dynamic change in ionic concentration and their interpretation is still rather difficult. Using ESM, Balke et al. studied silicon thin film anodes and reported higher ion concentrations in grain boundaries compared to the bulk.[16] For $LiCoO_2$ they found a temperature dependence of the ionic signal and dependency on the grain orientation.[23] Amanieu et al., Alikin et al., and Luchkin et al. calculated diffusion coefficients from their ESM measurements for $LiMnO_2$ and reported lower ionic concentration signals at the grain center. Guo et al. found a dependence of the diffusion coefficient on the location in the grains of $LiCoO_2$.[24] Chen et al. studied $LiFePO_4$ before and after cycling and reported a change in the signal depending on the preparation technique.[25] Romanyuk et al. studied polyvinylidene fluoride (PVDF) as a binder material for Li ion batteries with ESM. They concluded that the electroosmotic flow of the electrolyte is the main contribution to the ESM signal, which is dependent on the permeability of the binder material.[26] In addition, ESM simulations were proposed to help explain the origin of the signal.[27–29]

In this paper, we present a tailored ESM technique to visualize areas with high ionic mobility and generate diffusion coefficient mappings on the nanometer scale. The presented results regarding the ionic mobility at crystal steps are providing further insights for material scientists and researchers to work on nanoscale energy storage and conversion materials, since these materials are promising candidates

†Deceased.
*Electrochemical Society Member.
zE-mail: andreas.friedrich@dlr.de

to enhance the storage capacity in batteries. The generated mappings of diffusion coefficients can be of special interest for theoretical work regarding modelling of charge and discharge processes of batteries. Additionally, the ionic concentration distribution in single particles of battery electrodes is necessary to perform exact simulations and modelling.

Theoretical Background

Principle of tailored time domain ESM technique.—The tailored time domain ESM (t-ESM) technique uses a different approach compared to the originally published technique by Balke et al.[16] and was proposed as time domain measurements performed by Jesse et al.[30] In the original technique of Balke et al., an ac-voltage is applied between the tip and the sample, which is assumed to induce an oscillation of the ions in the solid sample. The oscillation of the ions induces an oscillating volume change and is transferred to the sample surface. Its movement is measured as deflection of the AFM tip. In the time domain measurement, a dc-voltage of several milliseconds is applied to the tip to induce a concentration change, which is tracked using the surface displacement amplitude at the ac-voltage frequency. To increase the sensitivity of the measurement, the signal can be amplified using the contact resonance frequency of the AFM tip with the sample-tip contact resonance frequency as the driving frequency of the applied ac-voltage. Since the contact resonance frequency is linked to the material properties and topography, it changes during the surface scan and needs to be tracked using a phase looked loop (PLL),[27,31,32] dual resonance frequency tracking (DRFT or DART),[25,33] or band excitation (BE).[23,34,35] Hence, errors in the tracking of the resonance frequency may lead to artefacts in the data. Using just a single frequency out of the contact resonance range leads to a lower amplification, but has the advantage that it is insensitive to material properties and topography crosstalk.

Underlying mechanisms leading to the surface expansion.— There are several mechanisms leading to an expansion of the surface as detected by ESM. The main mechanism is assumed to be the appearance of a *Vegard-strain* due to a change in ionic concentration.[36] Other mechanisms that can contribute are i) inverse piezoelectric effect, flexoelectric effect and electrostriction ii) deformation potential, electron-hole and electron-phonon coupling, iii) electrochemical reactions on the surface, iv) electrostatic influence and electric Lorenz-like forces and v) temperature related volume expansion.[15,27–29,37–39] Which of these effects attributes to the volume change is still under debate, more theoretical and model experiments are needed to facilitate a deeper understanding of the ESM signal and the contributing influences. Further explanations for the different mechanisms are given in the supplemental information. Nevertheless, even if the contributions of different mechanisms to the ESM signal is still a topic of research, its variation during and after a dc-voltage pulse is generally accepted to be induced by ionic concentration change due to diffusion and migration.

In a first approach, the relationship between the change in ionic concentration and the surface strain $\varepsilon_{i,j}$ is given by Hooks law in Equation 1.[37,40–43]

$$\varepsilon_{i,j} = \beta_{i,j} \, \delta c_{i,j}^{Li} + \frac{1+\nu}{E} \, \sigma_{i,j} \qquad [1]$$

The first term on the right-hand side $\beta_{i,j} \, \delta c_{i,j}^{Li}$ represents the chemical contribution to the strain, while the second term on the right-hand side $\frac{1+\nu}{E} \sigma_{i,j}$ represents the contribution of internal stress. In this case, $\beta_{i,j}$ is the Vegard expansion tensor, $\delta c_{i,j}^{Li}$ is the change in Li ion concentration, ν is the Poisson's ratio, E is the modulus of elasticity and $\sigma_{i,j}$ are the stress components. Other contributions to the surface strain were mentioned before, but are assumed to play a minor role and are neglected. Following the implications of Equation 1 with the assumption that the chemical component is the only relevant contribution to the surface strain, it can be concluded that the change in Li ion concentration $\delta c_{i,j}^{Li}$ is proportional to the resulting surface strain

$\varepsilon_{i,j}$. Morozovska et al. presented a general solution for the surface displacement $u_{i,j}$ based on the strain from Equation 1.[18] Their solution demonstrates that the surface displacement $u_{i,j}$ is proportional to the concentration change of the ionic species and dependent on the Vegard expansion tensor, which is expressed in Equation 2.[27]

$$u_{i,j} \propto \beta_{i,j} \, \delta c_{i,j}^{Li} \qquad [2]$$

Therefore, the resulting surface displacement amplitude is proportional to the change in Li ion concentration dc_{Li}, which is linked to the mobility of the ions in the material beneath the tip.[23,28,38] The change in surface displacement amplitude is therefore correlated to the change in ionic concentration, and in addition the transient behavior to the diffusion of the ions.

The measurement is divided in two time periods. In the first period the electric field is the driving force for the ionic movement, while at the same time, the concentration gradient is directed in the opposite direction of the electric field hindering the migration (migration/ diffusion). This yields an effective migration/ diffusion coefficient D1. In the second period, the driving force is the concentration gradient, which is induced by the increased/decreased local ion concentration built up by the migration in the first range and leads to a diffusion coefficient D2, which is solely caused by the concentration gradient.

$$c(x, t) = A_0 \exp\left(\frac{-x^2}{4Dt}\right) \qquad [3]$$

$$c^*(x, t) = a \exp(-b\, t) + c \qquad [4]$$

Local diffusion coefficients were extracted by fitting the data points retrieved from the expansion/retraction curves. The analytical solution for the diffusion calculated thereby is given in Equation 3 with the diffusion coefficient D and a pre-exponential component A_0. Jesse et al., Luchkin et al. and Guo et al. proposed an exponential behavior as it is seen in Equation 4.[24,28,30,44,45] The characteristic time constant with $b = \frac{1}{\tau_{x,y}}$ was retrieved using Equation 4, the diffusion coefficient was calculated using $D_{x,y} = \frac{l^2}{\tau_{x,y}}$. The characteristic length l is the tip radius.

Depending on the polarization, the local ionic concentration beneath the tip increases or decreases, accompanied by a surface expansion or contraction and is recorded by the vertical deflection of the tip. During the applied voltage pulse, migration and diffusion take place in opposite directions; after the applied voltage pulse relaxations takes place due to pure diffusion. With this set-up, the change of local ionic concentration and the dynamic movement of ions are mapped simultaneously. The dependence on time of the characteristic time constants for every image point delivers local information on the diffusion and migration of the ions in the material.

Experimental

Measurement set-up.—The experimental set-up used is shown in Figure 1a. A Bruker Icon system installed inside a glove box, equipped with PeakForce Mode and a Zurich Instruments (HF2LI) lock-in is used. As AFM probes Bruker SCM-PIT with a spring constant of 2.8 N/m and a resonance frequency of approximately 75 kHz were used. Voltage pulse generation and data recording was performed with a LabVIEW (V. 2016) routine on an additional computer. The voltage pulses were applied directly to the AFM tip using a modified PFM module with an amplitude of 3 V for the dc-voltage pulses and 2 V for the superimposed ac-excitation at 25 kHz. The dc-voltage induces the change in the ionic concentration, which is tracked using the amplitude of the oscillating surface at the ac-voltage frequency and further referred to as "surface displacement" with arbitrary units. The photodiode signals of the AFM were extracted using a Bruker break-out box (SAM V) and recorded with a National Instruments PCI card (NI 6111). The surface displacement signal is the real, in-phase signal amplitude (X) of the lock-in from the vertical deflection photo diode AFM signal. Morozovska et al. show, that the real part of the surface
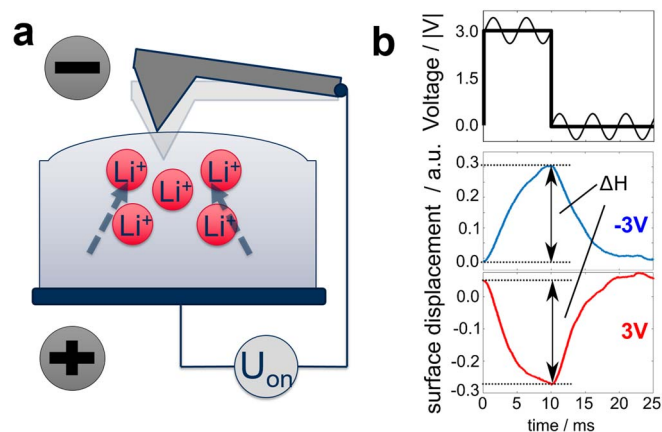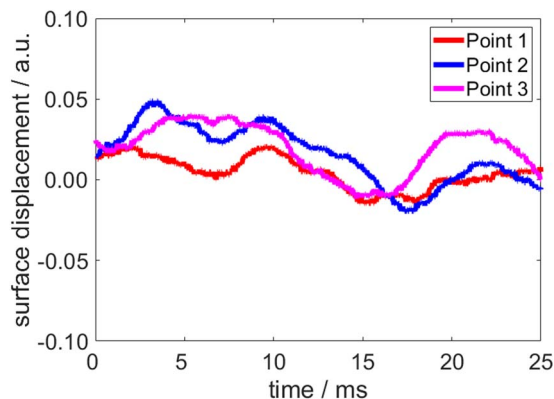
Figure 1. Measurement principle, a) scheme of set-up and mechanism of surface expansion, and b) applied dc- and ac-voltage profile in absolute values (top), leading to the surface expansion on Si/C with −3 V applied dc-voltage pulse (middle), and surface contraction with +3 V dc-voltage pulse (bottom).

Figure 2. Measurement curves of an intrinsic, non-lithiated silicon wafer surface with an applied voltage pulse of −3 V for 10 ms.

displacement is mainly determining the absolute signal, especially at lower frequencies for concentration driven processes, which corresponds to the dc-voltage off period of our measurement.[18,19] The proposed theory of Morozovska et al. is in agreement with our observation, namely the X signal showing nearly the same signal intensity compared to the amplitude R (Fig. S4).

The AFM measurements provide the two standard signals, the topography of the sample and the deflection error, which is the feedback signal of the control unit. The measurements are performed in contact mode with an additional interleave scan line. In the first scan line, the topography and deflection error are recorded as trace and retrace scans. This is the standard contact mode. In the second scan line, the tip scans the same location again. The voltage pulses are applied to the tip with a positive polarity during trace, and negative polarity during retrace. The standard scanning mode is not influenced by the applied potentials at the tip. The data analysis of the recorded AFM mappings was performed for every data point separately using MATLAB (Release 2018a).

Measurement of dynamic behavior.—An example of the recorded signal at one data point is given in Figure 1b for a measurement on Si/C electrodes. The surface displacement (ESM signal amplitude, which is extracted from the vertical photo diode signal as the response of the ac-voltage) is drawn against the time. The middle part gives the surface displacement during the negative applied voltage step, the lower part the surface displacement due to a positive applied voltage step. The surface displacement is indicated as ΔH, which is the signal amplitude difference from the beginning of the voltage pulse to the end of the voltage pulse. If not otherwise stated a voltage step of ±3 V was applied for 10 ms, and recorded for further 15 ms to include the relaxation process. During the negative polarization of the tip, Li ions are accumulating in the material and move toward the tip. In case of the positive polarization of the AFM tip, Li ions are migrating in the opposite direction, away from the AFM tip. Using this set-up, differences in the response of ion movement due to the polarity at the AFM tip are recorded at the same location.

Sample preparation & cycling.—Lab fabricated silicon-carbon (Si/C) anodes were used for the measurements. The anodes contained microcrystalline silicon, carbon black and carboxymethyl cellulose (CMC) as binder. For the cross-section measurements, a home-build cross-section holder was used. Before installing the anodes in the holder, the cross-section was cut using an unfocused argon ion beam (JEOL IB-19520CCP) to minimize the topographical crosstalk during the measurements (6 kV for 8 h). Since the cross-section holder is not a closed system, EC:PC (1:1 vol%, Sigma Aldrich) was chosen as

electrolyte due to its low vapor pressure to minimize the evaporation and to facilitate the cycling of the open cell. Cycling was done vs. Li/Li$^+$ between 2 V and 0.005 V with a current density of 3 μA cm^{-2} and a constant voltage step during lithiation until the current dropped below 2 μA cm^{-2}. After cycling the electrode for 68 cycles inside the cross-section holder, the electrode was washed in the cross-section holder with DMC and the entire cross-section holder was transferred into a vacuum chamber of the glove box and kept at room temperature under a vacuum of 0.1 bar for more than 15 h to evaporate the remaining electrolyte inside the pores of the electrode. The electrode remained inside the cell holder for the whole time.

Highly oriented pyrolytic graphite (HOPG, NT-MDT Spectrum Instruments) was cycled inside a Swagelok cell vs. Li/Li$^+$ at 2.8 V – 0.01 V with 4.1 μA cm^{-2} in 1 M LiPF6 in ethylene carbonate (EC, Sigma Aldrich) and dimethyl carbonate (DMC, Sigma Aldrich) (1:1 vol %) for 3 cycles and measured in lithiated state. After cycling, HOPG was washed with DMC to clean the surface from the electrolyte and dried for 12 h under vacuum at 0.1 bar and room temperature.

Results and Discussion

t-ESM measurements on a silicon wafer and on HOPG.—An intrinsic silicon wafer was examined to measure the surface change of non-lithiated crystalline silicon. Measurements at different positions are given in Figure 2. The curves in Figure 2 show neither a trend following the applied voltage pulse nor a relaxation following the voltage pulse but only noise. Similar results were obtained with polyether ether ketone (PEEK), an industrial high-duty polymer without any mobile ions such as the silicon wafer (results not shown here). During the recorded time interval, no expansion/contraction of the surface caused by the piezoelectric or flexoelectric effect was observed for piezoelectric materials such as Si that may influence the ESM measurements. Their magnitude was either too small to be detected or induced volume changes had already relaxed.

HOPG and carbon black was examined to study the influence of the conductivity-enhancing additive. Here we show the results of HOPG, the results of carbon black are similar and are given in the supplemental information (Fig. S3). Figure 3 shows the deflection error signal caused by the Li ion concentration change during a negative voltage pulse of −3 V at the tip (Figure 3a), the resulting Li ion concentration change (Figure 3b), and the local height change with time at different sample positions (Figure 3c). Areas with a higher surface expansion in Figure 3b partly correspond to specific surface features visible in Figure 3a, but occurred also at areas of flat HOPG layers (top of the image). Comparing the results from HOPG in Figure 3c and the Si wafer in Figure 2, the surface displacement of HOPG shows an influence of the applied voltage pulse and a subsequent relaxation. As expected from HOPG, the surface displacement due to the change of Li ion concentration is small (expected volume expansion due to
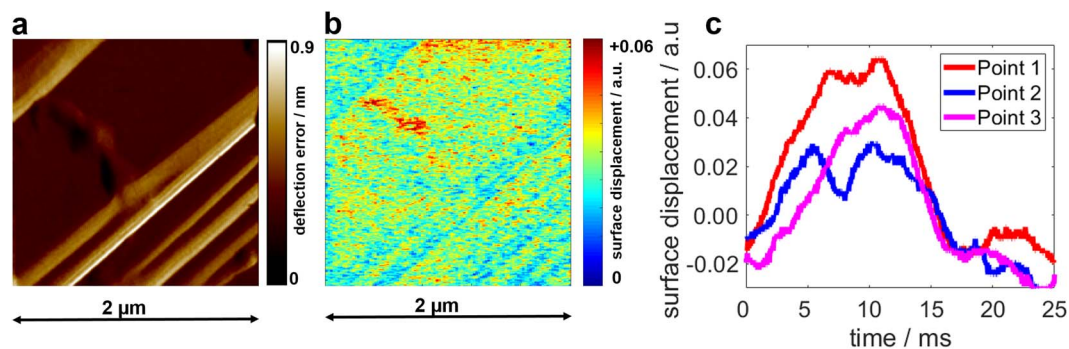
Figure 3. HOPG surface in lithiated state, a) deflection error, b) mapping of surface displacement due to the negative tip polarization, and c) volume change with time at different sample positions. Voltage pulse of −3 V for 10 ms.

lithiation of around 10%[46,47]) and the curves exhibit a small signal to noise ratio. Measurements on other locations of the HOPG sample gave similar results as on the non-lithiated Si wafer with no measureable surface displacement. Comparing these results with Figure 1b it can be concluded that for Si/C anodes, the lithiation of silicon is the main mechanism leading to the surface displacement. A contribution of the volume change of carbon black to a displacement to the overall signal is one order of magnitude smaller (0.06 a.u. for HOPG and 0.3 a.u. for the Si/C anode) and can be neglected. Furthermore, the carbon black layer thickness is much smaller than the HOPG sample, which further decreases the Li ion storage capacity and is limiting the possible concentration change in the carbon black layer.

Additionally, the fresh, non-lithiated Si/C anode was measured and the same results as for non-lithiated Si wafer are obtained (Figure S2). The results of the control experiments show, that only lithiated samples show a surface displacement signal. Nevertheless, the signal intensities of HOPG and carbon black are much smaller compared to the lithiated Si/C electrode, which leads us to conclude, that the main mechanism generating the signal is the ionic concentration change in the silicon.

Analysis of Li ion mobility in silicon composite electrode material.—Silicon composite anodes are a promising candidate as a next generation anode material but exhibit so far only low cycling stability due to their large volume expansion of up to 300% in fully lithiated state.[48,49] Figure 4 shows an example of the t-ESM measurement of the cross-section of an aged Si/C anode. For the grain structure after the cycling we assume a lithiated, amorphous silicon shell with a non-lithiated, crystalline silicon core. Cycling data and a comparison of the electrochemical behavior of the cross-section holder with the cycling in a Swagelok cell are provided in the supplemental information (Fig. S1). In Figure 4a, the deflection error mapping is shown. Figures 4b and 4c give the change in ionic concentration due to the applied positive and negative potential of ±3 V at the AFM tip. The surface contracted during the positive applied potential (Figure 4b), and expanded during the negative applied potential (Figure

4c). Since the height changes in Figures 4b and 4c show similar areas corresponding to large changes in ionic concentration, one can rule out significant topographic and tip-related contributions to the height change that may be caused by a variation in the tip-sample contact area to the measurement signal. Furthermore, artefacts due to the scan direction, i.e. by a different tip orientation and different tip-sample contact can be ruled out since the trace (Figure 4b) and retrace (Figure 4c) mappings are similar.[50]

The step, which runs diagonally across the image, is clearly visible in all three images. For Figures 4b and 4c, the step exhibits a higher change in ionic concentration compared to the grain centers, which is in agreement with results from other groups and due to the dependency of fast diffusion paths on the crystal orientation.[16,23,34,42] In Figures 5a and 5b, surface displacements over time at different sample positions marked in Figure 4c are plotted with the colors corresponding to the line colors in Figure 5. The curves in Figure 5a represent measurement points at the step, while Figure 5b shows measurement points inside the grains.

The higher signal intensity at the step can be explained by a higher mobility of ions compared to the grain interior. Assuming a homogeneous Li ion concentration across the grain and the step, a higher ionic mobility, due to a different crystal orientation at the step, will lead to a more pronounced surface displacement due to the faster change in concentration. This assumption is valid for the case that the maximum ion concentration was not reached by the applied voltage pulse. The interdependency of the ionic mobility and the crystal orientation is reported for layered $LiCoO_2$, V_2O_5, microcrystalline silicon and single crystal silicon.[23,45,51–54]

In addition to the ionic mobility, saturation of Li ion concentration can limit the surface displacement. Hence, the dependency of the surface displacement on the applied dc-voltage amplitude was studied. The same area was scanned with different dc-voltage pulse amplitudes. The resulting surface displacement maps are shown in Figure 6a. The magnitude of surface displacement at three spots was extracted and plotted over the corresponding dc-voltage, shown in Figure 6b. The dots were averaged over three adjacent data pixel and the error
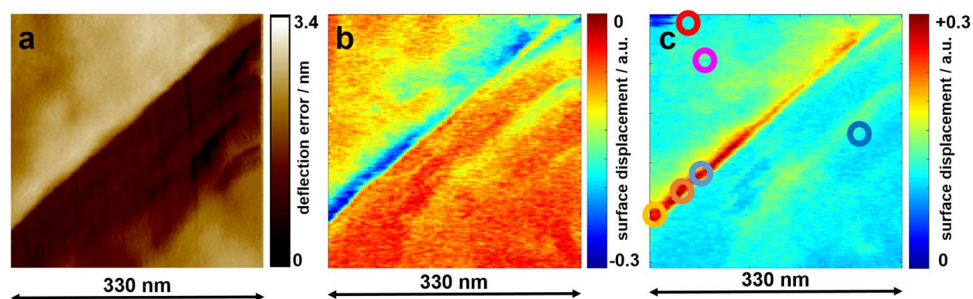
Figure 4. Aged silicon composite anode, a) deflection error mapping, b) surface displacement, trace with +3 V at the tip, and c) surface displacement, retrace with −3 V at the tip.
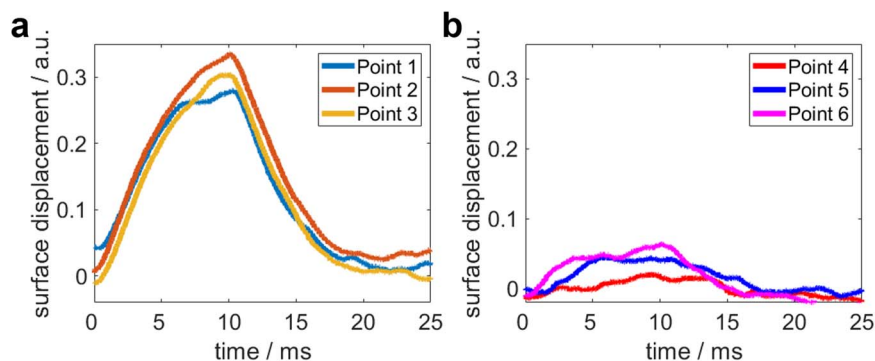
Figure 5. Extracted expansion curves at data acquisition points out of Figure 4c, a) data points with a high surface displacement at the step, and b) with lower or no surface displacement moving away from the step. The dc-voltage of −3 V was applied for 10 ms.

bars give the standard deviation. The overall surface displacement of all data points in the image is plotted as a histogram in Figure 6c. For all three positions, the displacement is the same for −3 V pulse amplitude, a significant height increase occurred for all positions upon a voltage step from −3 to −5 V. At point 1, a saturation of the height change is achieved with −5 V; a further increase of the voltage does not increase the surface displacement any more. At point 2, the surface displacement increased linearly up to −6 V and slightly drops for a higher applied voltage. At point 3 an increase from −3 to −5 V and a further decrease for higher voltages is visible. The histograms of all surface displacement values of the different dc-voltage pulse amplitudes (Figure 6c) indicate that the distribution broadens, leading to an increase of the overall amount of higher surface displacement counts with increasing dc-voltage amplitude, while the peak height of the distribution decreased and shifts toward higher values for the surface displacement. The resulting measured surface displacements reflects a steady-state between an increase of ion concentration generated by the electric field and an increasing velocity of back-diffusion due to the higher concentration gradient. These two opposite effects result in a net surface displacement, which depends on the relative contribution of each effect. The steady rise of the net peak height of the surface displacement in Figure 6b indicates the increase of migration over the increase of back diffusion. At the same time, the levelling or decrease of net peak height (point 1 and 3) of the surface displacement with higher voltage at the same positions in Figure 6b must be caused by

higher back-diffusion compared to migration. The shift of the peak position of point 2 to higher voltages indicates a higher ion saturation at this position before back-diffusion starts to predominate. The migration process cannot maintain the ionic flow toward the surface and back-diffusion starts to dominate. Another possible explanation for the decrease of the surface displacement with increasing voltage amplitude could be irreversible concentration or structural changes inside the probed volume. There are no visible surface changes after the measurements, therefore no surface reactions occurred, which could influence the kinetic properties. However, changes inside the material cannot be ruled out. Yang et al. reported a similar behavior for $LiCO_2$ with decreasing ESM signal over several measurements of the same location. They assume irreversible concentration changes inside the material and decreased activity of Li ions.[55]

Nevertheless, for the measurements shown in Figure 4, which are performed with a dc-voltage of −3 V, the results from Figure 6 validate that a saturation concentration in the material was not reached. Therefore, the different surface displacements are a result of a difference in ionic mobility and not limited by the ion concentration.

Calculation of local diffusion coefficients for a silicon composite electrode.—As described above, the dynamic response of the surface displacement delivers information on the dynamics of the ionic movement inside the material. Diffusion and migration/diffusion coefficients are extracted by fitting an exponential curve to the data points
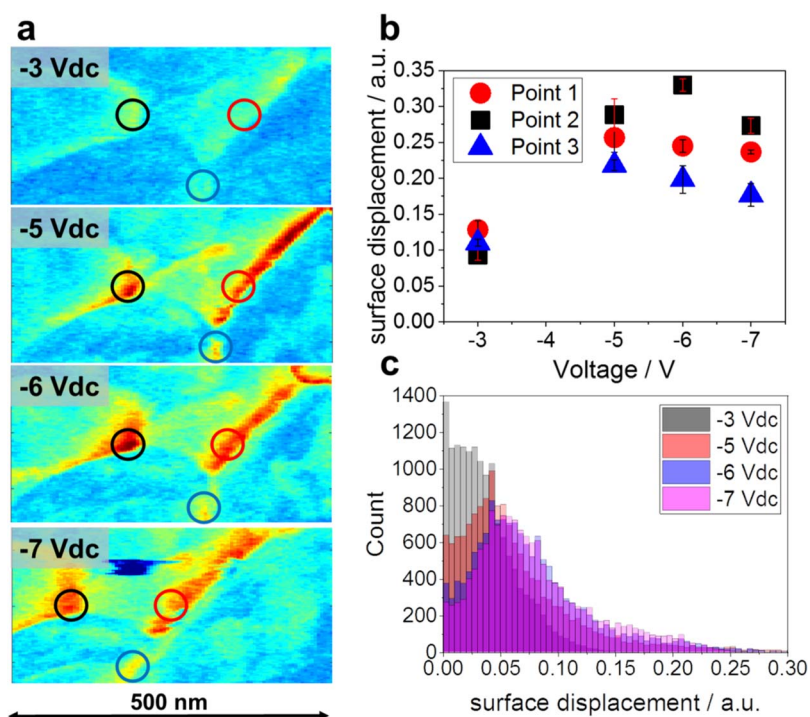
Figure 6. Resulting surface displacement for different applied voltages, a) mappings of surface expansion, b) surface expansion at data points marked in (a), and c) histogram of surface displacements of all measured image points. Point 1 is marked in red, point 2 is marked in black and point 3 is marked in blue.
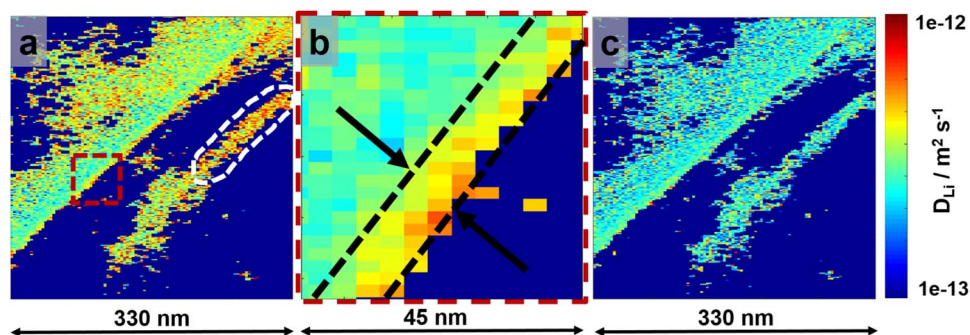
Figure 7. Mappings of calculated coefficients D1 and D2 at same location as in Figure 4, a) diffusion coefficient due to concentration gradient after voltage pulse of −3 V, b) zoom into marked area of step in (a), and c) effective migration/diffusion coefficient due to the electric field during voltage pulse and simultaneous back diffusion.

for each of the two time periods. Some examples for the fitting results are given in Figure S5.

Data fitting was limited to data points with at least 15% surface displacement of the maximum value. This threshold reduced the amount of diffusion coefficients extracted out of the measured data, but ensured the validity of the fitting process. Figure 7 presents a mapping of the resulting diffusion coefficients. Figure 7a gives the diffusion coefficients D2 calculated from the data points after the applied voltage pulse and solely governed by the concentration gradient. The mapping of the effective migration coefficient D1 that is reduced by back diffusion is shown in Figure 7c. Both coefficients are in the range of around 10^{-14} to 10^{-12} m^2 s^{-1}, which is within the range, but at the lower bound of diffusion coefficients reported for silicon in the literature and close to theoretical values given by Johari et al.[17,30,56–59] The differences of the diffusion coefficient compared to literature values can be explained by the dependence of the diffusion coefficient on the used diffusion length, which is assumed to be the tip radius due to the penetration of the electric field inside the material.[16,30,60] A short discussion about the discrepancies of the experimentally determined diffusion coefficients for silicon was done by Ozanam and Russo.[51] The distribution of the diffusion coefficients shows higher coefficients around $1 \cdot 10^{-12}$ m^2 s^{-1} at the step and at some positions away from the step. Moving away from the step, the coefficients decrease toward approximately $6 \cdot 10^{-13}$ m^2 s^{-1} and slightly increase again, visible in the top left of Figure 7a. Part of the step from the marked red square is shown in the zoom of Figure 7b and exhibits a thickness of approximately 12 nm. The white marked area in Figure 7a shows a second step of approximately 35 nm, which exhibits similar diffusion coefficients as the step in Figure 7b. The higher diffusivity at the step points toward a preferential material structure for the diffusion of ions, which

is presumably more amorphous, since amorphous silicon is expected to have a higher diffusivity compared to crystalline silicon.[57,61]

In contrast, ESM time spectroscopy results of Guo et al. on LiCoO$_2$, and Jesse et al. on amorphous silicon report lower diffusion coefficient of the grain boundaries compared to the grains itself.[24,30] The different results might be explained by the significant difference in material structure with different properties of the grain boundaries, which leads to differences in Li ion concentration and mobility.

A comparison of the diffusion coefficients during the voltage pulse in Figure 7c (D1) and after the voltage pulse (D2) in Figure 7a exhibits lower effective diffusion coefficients for the migration/diffusion process D1 compared to the concentration gradient-driven diffusion leading to D2. The histogram in Figure 8 visualizes the histograms for D1 and D2 regarding all image points above the threshold. The peak for the migration driven process reaches the maximum counts near $2 \cdot 10^{-13}$ m^2 s^{-1}, while the concentration gradient driven process has a larger maximum near $4 \cdot 10^{-13}$ m^2 s^{-1}. This difference is expected because for the migration driven process a steady-state of migration and oppositely directed back-diffusion arises. The built-up concentration gradient due to the electric field hinders the further movement of the ions, therefore decreases the diffusion coefficient during the migration-driven process and leads to smaller coefficients D1 compared to D2. These results indicate that the solid-state migration of ions has a similar velocity range as the solid-state diffusion if the electric field is strong enough.

Conclusions

We presented a tailored ESM technique to visualize the ionic concentration change in the sample volume under the AFM tip and recorded the dynamics of ionic diffusion. For silicon composite anodes, the signal emerged from the Li ion concentration change in the silicon particles; further contributions such as piezoelectricity or flexoelectricity had no significant influence. The results indicated a higher ionic mobility at the step, probably due to a different material structure. Analysis of the dc-voltage amplitude dependence showed a saturation of the surface displacement at high dc-voltages due to concentration limitations inside the material or irreversible concentration change in the probed volume. Using the measurement curves, diffusion coefficients were calculated and the resulting values are consistent with literature values. The benefit of the technique is the ability to generate mappings of local diffusion coefficients on the nanometer scale. The results present strong variations of the diffusion coefficient within one grain.
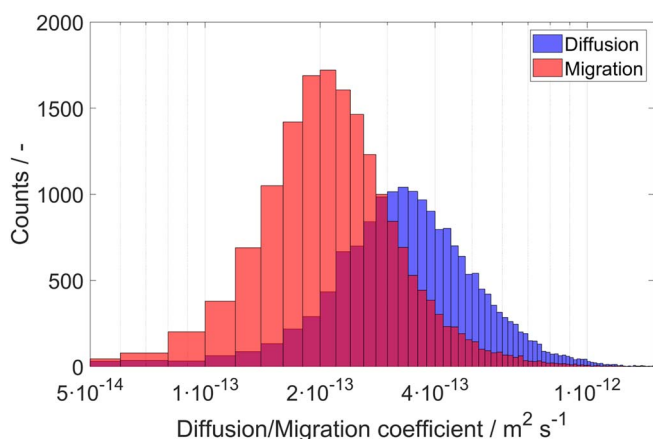
Figure 8. Distribution of diffusion coefficients of all image points above the threshold for D1 (red) and D2 (blue).

ORCID

M. Simolka https://orcid.org/0000-0003-4613-1236
K. A. Friedrich https://orcid.org/0000-0002-2968-5029
R. Hiesgen https://orcid.org/0000-0002-0246-4509

References

1. F. J. Giessibl, *Science*, **267**, 68 (1995).
2. D. Aurbach, H. Teller, M. Koltypin, and E. Levi, *Journal of Power Sources*, **119–121**, 2 (2003).
3. D. Aurbach and Y. Cohen, *Journal of the Electrochemical Society*, **143**, 3525 (1996).
4. D. Aurbach, B. Markovsky, M. D. Levi, E. Levi, A. Schechter, M. Moshkovich, and Y. Cohen, *Journal of Power Sources*, **81**, 95 (1999).
5. Y. S. Cohen, Y. Cohen, and D. Aurbach, *J. Phys. Chem. B*, **104**, 12282 (2000).
6. R. Hiesgen, S. Sörgel, R. Costa, L. Carlé, I. Galm, N. Cañas, B. Pascucci, and K. A. Friedrich, *Beilstein Journal of Nanotechnology*, **4**, 611 (2013).
7. R. Elazari, G. Salitra, Y. Talyosef, J. Grinblat, C. Scordilis-Kelley, A. Xiao, J. Affinito, and D. Aurbach, *J. Electrochem. Soc.*, **157**, A1131 (2010).
8. T. Doi, M. Inaba, H. Tsuchiya, S.-K. Jeong, Y. Iriyama, T. Abe, and Z. Ogumi, *Journal of Power Sources*, **180**, 539 (2008).
9. Q. P. McAllister, K. E. Strawhecker, C. R. Becker, and C. A. Lundgren, *Journal of Power Sources*, **257**, 380 (2014).
10. A. Clémençon, A. T. Appapillai, S. Kumar, and Y. Shao-Horn, *Electrochimica Acta*, **52**, 4572 (2007).
11. J. Zhu, K. Zeng, and L. Lu, *Journal of Applied Physics*, **111**, 063723 (2012).
12. L. Martin, H. Martinez, M. Ulldemolins, B. Pecquenard, and F. Le Cras, *Solid State Ionics*, **215**, 36 (2012).
13. D. Abraham, J. Liu, C. Chen, Y. Hyung, M. Stoll, N. Elsen, S. MacLaren, R. Twesten, R. Haasch, E. Sammann, I. Petrov, K. Amine, and G. Henriksen, *Journal of Power Sources*, **119–121**, 511 (2003).
14. M. Broussely, P. Biensan, F. Bonhomme, P. Blanchard, S. Herreyre, K. Nechev, and R. J. Staniewicz, *Journal of Power Sources*, **146**, 90 (2005).
15. A. N. Morozovska, E. A. Eliseev, A. K. Tagantsev, S. L. Bravina, L.-Q. Chen, and S. V. Kalinin, *Physical Review B*, **83** (2011).
16. N. Balke, S. Jesse, A. N. Morozovska, E. Eliseev, D. W. Chung, Y. Kim, L. Adamczyk, R. E. García, N. Dudney, and S. V. Kalinin, *Nature Nanotechnology*, **5**, 749 (2010).
17. N. Balke, S. Jesse, Y. Kim, L. Adamczyk, A. Tselev, I. N. Ivanov, N. J. Dudney, and S. V. Kalinin, *Nano Letters*, **10**, 3420 (2010).
18. A. N. Morozovska, E. A. Eliseev, N. Balke, and S. V. Kalinin, *Journal of Applied Physics*, **108**, 053712 (2010).
19. A. N. Morozovska, E. A. Eliseev, and S. V. Kalinin, *Applied Physics Letters*, **96**, 222906 (2010).
20. A. Eshghinejad, E. Nasr Esfahani, P. Wang, S. Xie, T. C. Geary, S. B. Adler, and J. Li, *Journal of Applied Physics*, **119**, 205110 (2016).
21. E. Nasr Esfahani, A. Eshghinejad, Y. Ou, J. Zhao, S. Adler, and J. Li, *Microscopy Today*, **25**, 12 (2017).
22. S. Y. Luchkin, H.-Y. Amanieu, D. Rosato, and A. L. Kholkin, *Journal of Power Sources*, **268**, 887 (2014).
23. N. Balke, S. Kalnaus, N. J. Dudney, C. Daniel, S. Jesse, and S. V. Kalinin, *Nano Letters*, **12**, 3399 (2012).
24. S. Guo, S. Jesse, S. Kalnaus, N. Balke, C. Daniel, and S. V. Kalinin, *Journal of the Electrochemical Society*, **158**, A982 (2011).
25. Q. Nataly Chen, Y. Liu, Y. Liu, S. Xie, G. Cao, and J. Li, *Applied Physics Letters*, **101**, 063901 (2012).
26. K. Romanyuk, C. M. Costa, S. Y. Luchkin, A. L. Kholkin, and S. Lanceros-Méndez, *Langmuir*, **32**, 5267 (2016).
27. H.-Y. Amanieu, H. N. M. Thai, S. Y. Luchkin, D. Rosato, D. C. Lupascu, M.-A. Keip, J. Schröder, and A. L. Kholkin, *Journal of Applied Physics*, **118**, 055101 (2015).
28. S. Y. Luchkin, K. Romanyuk, M. Ivanov, and A. L. Kholkin, *Journal of Applied Physics*, **118**, 072016 (2015).
29. D. O. Alikin, A. V. Ievlev, S. Y. Luchkin, A. P. Turygin, V. Y. Shur, S. V. Kalinin, and A. L. Kholkin, *Applied Physics Letters*, **108**, 113106 (2016).
30. S. Jesse, N. Balke, E. Eliseev, A. Tselev, N. J. Dudney, A. N. Morozovska, and S. V. Kalinin, *ACS Nano*, **5**, 9682 (2011).
31. Q. N. Chen, S. B. Adler, and J. Li, *Applied Physics Letters*, **105**, 201602 (2014).
32. Q. N. Chen, Y. Ou, F. Ma, and J. Li, *Applied Physics Letters*, **104**, 242907 (2014).
33. J. Li, J.-F. Li, Q. Yu, Q. N. Chen, and S. Xie, *Journal of Materiomics*, **1**, 3 (2015).
34. N. Balke, E. A. Eliseev, S. Jesse, S. Kalnaus, C. Daniel, N. J. Dudney, A. N. Morozovska, and S. V. Kalinin, *Journal of Applied Physics*, **112**, 052020 (2012).
35. S. Jesse, A. Kumar, T. M. Arruda, Y. Kim, S. V. Kalinin, and F. Ciucci, *MRS Bulletin*, **37**, 651 (2012).
36. L. Vegard, *Zeitschrift für Physik A Hadrons and Nuclei*, **5**, 17 (1921).
37. S. V. Kalinin and A. N. Morozovska, *Journal of Electroceramics*, **32**, 51 (2014).
38. N. Schön, D. C. Gunduz, S. Yu, H. Tempel, R. Schierholz, and F. Hausen, *Beilstein Journal of Nanotechnology*, **9**, 1564 (2018).
39. V. Lushta, S. Bradler, B. Roling, and A. Schirmeisen, *Journal of Applied Physics*, **121**, 224302 (2017).
40. A. Tselev, A. N. Morozovska, A. Udod, E. A. Eliseev, and S. V. Kalinin, *Nanotechnology*, **25**, 445701 (2014).
41. X. Zhang, A. M. Sastry, and W. Shyy, *Journal of The Electrochemical Society*, **155**, A542 (2008).
42. D.-W. Chung, N. Balke, S. V. Kalinin, and R. E. García, *Journal of The Electrochemical Society*, **158**, A1083 (2011).
43. H. Dal and C. Miehe, *Computational Mechanics*, **55**, 303 (2015).
44. K. G. F. Janssens, Ed., *Computational materials engineering: an introduction to microstructure evolution*, p. Online Ressource, Academic Press, Amsterdam; Heidelberg [u.a.], (2007) http://www.sciencedirect.com/science/book/9780123694683.
45. P. G. Shewmon, *Diffusion in solids*, 2.ed., p. 246, Minerals, Metals & Materials Society, Warrendale, Pa, (1989).
46. N. Nitta, F. Wu, J. T. Lee, and G. Yushin, *Materials Today*, **18**, 252 (2015).
47. Y. Qi and S. J. Harris, *J. Electrochem. Soc.*, **157**, A741 (2010).
48. B. A. Boukamp, G. C. Lesh, and R. A. Huggins, *J. Electrochem. Soc.*, **128**, 725 (1981).
49. L. Baggetto, R. A. H. Niessen, F. Roozeboom, and P. H. L. Notten, *Advanced Functional Materials*, **18**, 1057 (2008).
50. B. Voigtländer, *Scanning probe microscopy*, Springer Berlin Heidelberg, New York, NY, (2015).
51. F. Ozanam and M. Rosso, *Materials Science and Engineering: B*, **213**, 2 (2016).
52. M. Pharr, K. Zhao, X. Wang, Z. Suo, and J. J. Vlassak, *Nano Letters*, **12**, 5039 (2012).
53. S. W. Lee, M. T. McDowell, J. W. Choi, and Y. Cui, *Nano Letters*, **11**, 3034 (2011).
54. M. E. Garcia and S. H. Garofalini, *J. Electrochem. Soc.*, **146**, 840 (1999).
55. S. Yang, B. Yan, T. Li, J. Zhu, L. Lu, and K. Zeng, *Phys. Chem. Chem. Phys.*, **17**, 22235 (2015).
56. M. Wang, X. Xiao, and X. Huang, *Journal of Power Sources*, **307**, 77 (2016).
57. P. Johari, Y. Qi, and V. B. Shenoy, *Nano Letters*, **11**, 5494 (2011).
58. R. Ruffo, S. S. Hong, C. K. Chan, R. A. Huggins, and Y. Cui, *The Journal of Physical Chemistry C*, **113**, 11390 (2009).
59. G. A. Tritsaris, K. Zhao, O. U. Okeke, and E. Kaxiras, *The Journal of Physical Chemistry C*, **116**, 22212 (2012).
60. A. Schirmeisen, A. Taskiran, H. Fuchs, B. Roling, S. Murugavel, H. Bracht, and F. Natrup, *Applied Physics Letters*, **85**, 2053 (2004).
61. N. Ding, J. Xu, J. Y. Yao, G. Wegner, X. Fang, C. H. Chen, and I. Lieberwirth, *Solid State Ionics*, **180**, 222 (2009).